AAS 19-919

CONTROL AND SIMULATION OF A DEPLOYABLE ENTRY VEHICLE WITH AERODYNAMIC CONTROL SURFACES

Benjamin W. L. Margolis[*], Wendy A. Okolo[†], Ben E. Nikaido[‡], Jeffrey D. Barton[§], Sarah N. D'Souza[¶]

In this paper, we investigate the static stability of a deployable entry vehicle called the Lifting Nano-ADEPT and design a control system to follow bank angle, angle-of-attack, and sideslip guidance commands. The control design, based on linear quadratic regulator optimal techniques, utilizes aerodynamic control surfaces to track angle-of-attack, sideslip angle, and bank angle commands. We demonstrate, using a nonlinear simulation environment, that the controller is able to accurately track step commands that may come from a guidance algorithm.

INTRODUCTION

The need to land high mass payloads and return samples from other planets is driving the development of innovative entry vehicle systems called Deployable Entry Vehicles (DEVs). DEVs are entry vehicles which have a thermal protection system that can stow into a smaller volume for launch and deploy prior to entry. NASA's Space Technology Mission Directorate (STMD) has successfully developed two types of DEVs, one that deploys mechanically (Adaptive Deployable Entry and Placement Technology - ADEPT) and another that deploys pneumatically (Hypersonic Inflatable Aerodynamic Decelerator - HIAD).[1] DEVs have the potential to deliver an equivalent science payload with a stowed diameter 3 to 4 times smaller than a traditional entry system with a rigid aeroshell.[1]

Traditional entry vehicles rely on reaction control systems mounted on the back shell to achieve guidance commands. In contrast, DEVs have no back shell, thus one of the primary design challenges for DEVs is the placement and integration of control systems. To address this challenge, STMD is funding Pterodactyl, a design, test, and build capability to (i) advance the current state of the art for entry vehicle guidance and control (G&C) and (ii) determine the feasibility of control system integration for various entry vehicle types, for example, those without a back shell.[2] This capability is currently being used to develop novel and non-propulsive G&C solutions for the Lifting Nano-ADEPT (LNA) vehicle.

[*]Aerospace Engineer Trainee, Systems Analysis Office, Aeronautics Directorate, NASA Ames Research Center, Moffett Field, CA, 94035

[†]Aerospace Research Engineer, Intelligent Systems Division, NASA Ames Research Center, Moffett Field, CA, 94035

[‡]Aerospace Engineer, Systems Analysis Office, Aeronautics Directorate, NASA Ames Research Center, Moffett Field, CA, 94035

[§]Guidance & Control Engineer, Force Projection Sector, John Hopkins University Applied Physics Laboratory, Laurel, MD, 20723

[¶]Aerospace Engineer, Systems Analysis Office, Aeronautics Directorate, NASA Ames Research Center, Moffett Field, CA, 94035

In this paper, we detail our efforts on the Pterodactyl project to design a control system that will utilize aerodynamic surfaces to track reference angle-of-attack and sideslip angle commands from a guidance algorithm. First, we provide a brief overview of the vehicle followed by the linear and angular dynamic and kinematic equations of motion of the vehicle. Next, we present the model of the aerodynamic forces and moments of the LNA and their dependencies on Mach number, angle-of-attack, and sideslip angle. Using the aerodynamic force and moment coefficients, we then investigate the lateral and longitudinal static stability of the vehicle. Next, we describe the novel control design architecture using eight control surfaces, depicted in Figure 1, to track guidance commands. Finally, simulation results showing the tracking of step-commands in angle-of-attack, and sideslip angle for a fixed bank angle are shown.

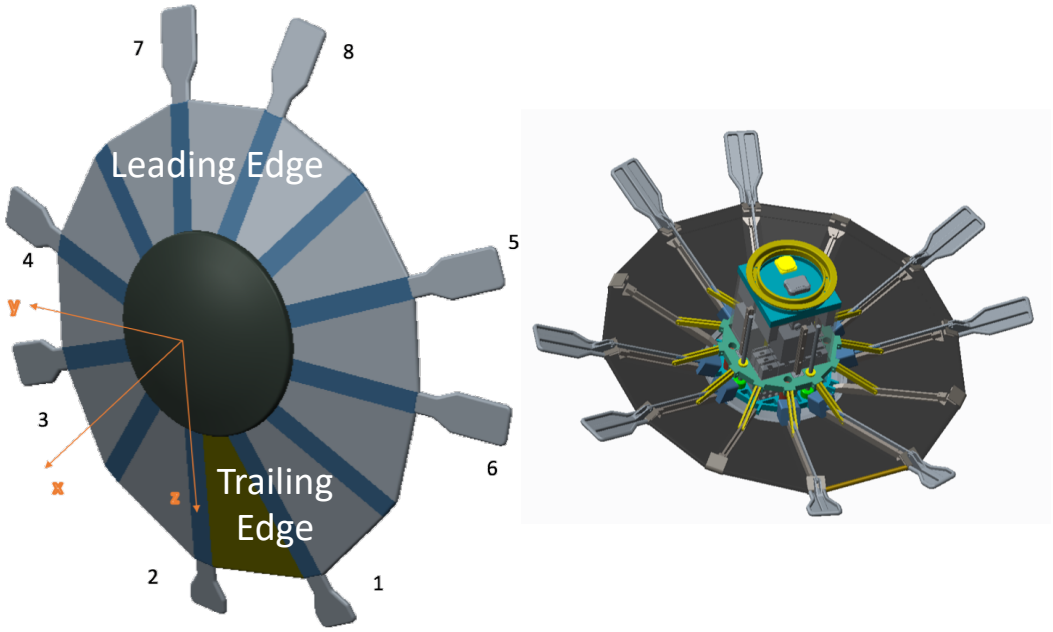

Figure 1: Fore and aft views of Lifting Nano-ADEPT vehicle with control surfaces

VEHICLE OVERVIEW

The LNA vehicle is a version of the ADEPT vehicle architecture. The ADEPT architecture features a flexible thermal protection system material attached to hinging ribs to form a heat shield that can be stowed during launch and deployed prior to entry.[1] This particular ADEPT realization has a nominal 1-meter diameter with two longer ribs on the trailing edge side of the vehicle to create an asymmetric surface. In the lift-up configuration, these ribs point downward to increase the lift-to-drag ratio.

For this study, aerodynamic control surfaces were attached to eight of the ribs as shown in Figure 1. The control surfaces used in this study were designed to provide maximal control authority while satisfying packaging and stowage requirements for a conceptual mission operation as outlined in a previous report.[2] The eight control surfaces are placed in pairs to prevent generating additional asymmetries and coupling based on the orientation of the ribs, to increase control authority, and to provide redundancy.

The control surfaces hinge into and out of the flow with 0 deflection defined as parallel to the attached rib, a positive deflection defined as deflection into the flow, and a negative deflection as deflection out of the flow. The design has deflection limits of -45 degrees to +25 degrees for all control surfaces.

The control surface configuration was designed with two pairs of longitudinal control surfaces to induce pitch moments and two pairs of lateral control surfaces to induce yaw moments. The body fixed coordinate system used here is the standard forward-right-down frame with x coming forward out of the nose of the vehicle, z perpendicular, pointing "down" between the two longer ribs, and y completing the right-handed coordinate system. Using this coordinate system, if the "top" longitudinal tabs labeled 7 and 8 deflect into the flow they will generate a positive pitch moment causing the vehicle to pitch upwards, moving the angle-of-attack in the positive direction. The "bottom" longitudinal tabs labeled 1 and 2 deflecting into the flow will generate a negative pitch moment, causing the vehicle to pitch downwards, moving the angle-of-attack in the negative direction. Similarly, the lateral tabs on the right labeled 3 and 4, when deflected into the flow, will induce a positive yaw moment, causing the vehicle to yaw right, corresponding to a negative sideslip. Finally, lateral tabs labeled 5 and 6 deflecting into the flow will induce a negative yaw moment, causing the vehicle to yaw left, corresponding to a positive sideslip.

EQUATIONS OF MOTION

In this section, we present the equations of motion of the hypersonic re-entry vehicle as described by Vinh.[3] The linear dynamics ignoring planet rotation are given by

$$\begin{aligned}
\dot{V} &= -\frac{g\left(z\right)}{m}\sin\left(\gamma\right) - \frac{1}{m}D \\
\dot{\gamma} &= \left(-\frac{g\left(z\right)}{m\,V} + \frac{V}{z}\right)\cos\left(\gamma\right) + \frac{1}{m\,V}\left(L\,\cos\left(\sigma\right) - S\,\sin\left(\sigma\right)\right) \\
\dot{\xi} &= \frac{1}{m\,V\,\cos\left(\gamma\right)}\left(L\,\sin\left(\sigma\right) + S\,\cos\left(\sigma\right)\right)
\end{aligned}$$

where V is the velocity of the vehicle, γ is the vehicle flight-path angle, ξ is the vehicle heading angle defined from due North, L, D, and S are the aerodynamic lift, drag, and side forces, respectively, $g\left(z\right)$ is the force due to gravity, dependent on the radial distance from the planet center z, σ is the bank angle, and m is the mass of the vehicle.

The angular dynamics are given by

$$\begin{bmatrix}\dot{p}\\ \dot{q}\\ \dot{r}\end{bmatrix} = \left(\mathbb{I}_b^{B/B_{cm}}\right)^{-1}\left(\begin{bmatrix}\mathcal{L}\\ \mathcal{M}\\ \mathcal{N}\end{bmatrix} - \begin{bmatrix}p\\ q\\ r\end{bmatrix} \times \mathbb{I}_b^{B/B_{cm}}\begin{bmatrix}p\\ q\\ r\end{bmatrix}\right)$$

where p, q, and r are the angular velocities about the body-fixed x, y, and z axes respectively, $\mathbb{I}_b^{B/B_{cm}}$ is the inertia tensor of the vehicle about its center of mass expressed in the body coordinates and $\mathcal{L}$, $\mathcal{M}$, and $\mathcal{N}$ are the aerodynamic roll, pitch, and yaw moments, respectively.

The angular kinematics are defined by

$$\begin{aligned}
\dot{\sigma} &= p\,\cos\left(\alpha\right)\,\sec\left(\beta\right) + r\,\sin\left(\alpha\right)\,\sec\left(\beta\right) \\
\dot{\alpha} &= -p\,\cos\left(\alpha\right)\,\tan\left(\beta\right) + q - r\,\sin\left(\alpha\right)\,\tan\left(\beta\right) \\
\dot{\beta} &= p\,\sin\left(\alpha\right) - r\,\cos\left(\alpha\right)
\end{aligned}$$

where α is the angle-of-attack and β is the sideslip angle. Finally, the linear kinematics are given by

$$\begin{aligned}
\dot{z} &= V \sin(\gamma) \\
\dot{\Phi} &= \frac{V}{z} \cos(\gamma) \cos(\xi) \\
\dot{\lambda} &= \frac{V}{z \cos(\Phi)} \cos(\gamma) \sin(\xi)
\end{aligned}$$

where Φ and λ are the latitude and longitude of the vehicle, respectively. The dynamic and kinematic variables are illustrated in Figures 2 and 3.

The aerodynamic forces and moments are assumed to be dependent on the angle-of-attack and sideslip as well as the Mach number M and control surface deflections δ_1, ..., δ_8 defined in the previous section. The aerodynamic forces and moments are of the form

$$F = \overline{q} S_A C_{(\cdot)} (\alpha, \beta, M, \delta_1, \ldots, \delta_8)$$

and

$$T = \overline{q} S_A \, \overline{c} \, C_{(\cdot)} (\alpha, \beta, M, \delta_1, \ldots, \delta_8)$$

respectively, where $C_{(\cdot)}$ are the dimensionless aerodynamic force and moment coefficients, S_A is the reference surface area, $\overline{c}$ is a reference length, $\overline{q}$ is the dynamic pressure defined by

$$\overline{q} = \frac{1}{2} \rho V^2$$

with ρ the altitude-dependent atmospheric density.

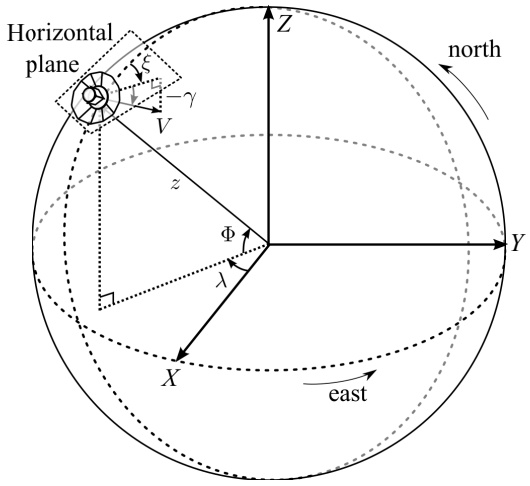

Figure 2: The position of the vehicle relative to the planet center

AERODYNAMIC DATABASE AND STATIC STABILITY

The aerodynamic force and moment coefficients for the vehicle were generated using Cart3D[4] for a matrix of flight conditions from the expected flight envelope. The values of the independent

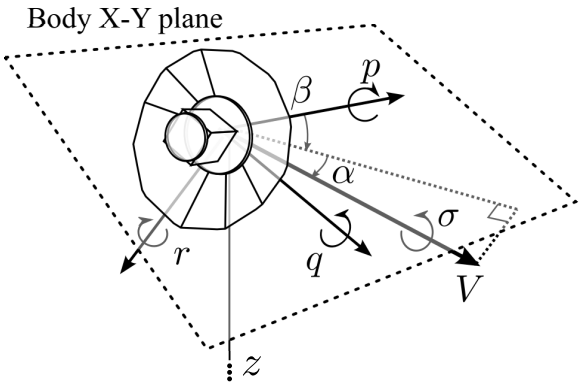

Figure 3: The orientation of the vehicle relative to the velocity vector

variables used to construct the database are listed in Table 1. Figure 4 depicts the aerodynamic force and moment coefficients as functions of angle-of-attack and sideslip for $M = 40$ of the base aeroshell (without control surfaces). The longitudinal coefficients C_L and $C_{\mathcal{M}}$ vary primarily with angle-of-attack while the lateral and directional coefficients C_S, $C_{\mathcal{L}}$, and $C_{\mathcal{N}}$ vary primarily with sideslip. For blunt-body entry vehicle geometry such as this, pitching down (decreasing angle-of-attack) generates positive lift up and the drag coefficient C_D is largest when the body centerline is aligned with the wind maximizing the surface area into the wind. In Figure 5, we show the longitudinal force and moment coefficients as functions of Mach and angle-of-attack and the lateral-directional force and moment coefficients as functions of Mach and sideslip. We include this to highlight the much smaller dependence of the aerodynamic coefficients on Mach than attitude.

Table 1: Flight conditions used to construct aerodynamic database

independent variable	values
Mach number M	{40, 31, 20, 15, 10, 5, 2}
angle-of-attack α, deg	{0, $\pm$5, $\pm$10, $\pm$15, $\pm$20}
sideslip angle β, deg	{0, $\pm$5, $\pm$10, $\pm$20}
control surface deflection δ_i, deg	{-45, -20, 0, 10, 20, 30}

To assess the vehicle stability and utilize the vehicle's aerodynamic data in simulation, multivariate B-splines[5] were constructed to smoothly interpolate the aerodynamic database at any Mach, angle-of-attack, sideslip angle, and control surface deflections. In Figures 6 – 8, we show the data points and interpolating splines for the roll, pitch, and yaw moment coefficients at $M = 40$ with tabs set parallel to the ribs ($\delta_1 = \delta_2 = \cdots = \delta_8 = 0\,\text{deg.}$) The interpolating spline curves can also be differentiated to obtain dimensionless static stability derivatives such as the dihedral effect, $C_{\mathcal{L}_\beta}$, the pitch stiffness, $C_{\mathcal{M}_\alpha}$, and the yaw stiffness, $C_{\mathcal{N}_\beta}$. Each stability derivative is defined as the derivative of the coefficient of the moment indicated by the first subscript with respect to the variable of the second subscript. In Figures 9 – 11, we show the stability derivatives for the same flight conditions. For lateral stability in roll, the dihedral effect should be negative, which is the case for this vehicle as shown in Figure 9. Note that even though the curves in Figure 9 show seemingly

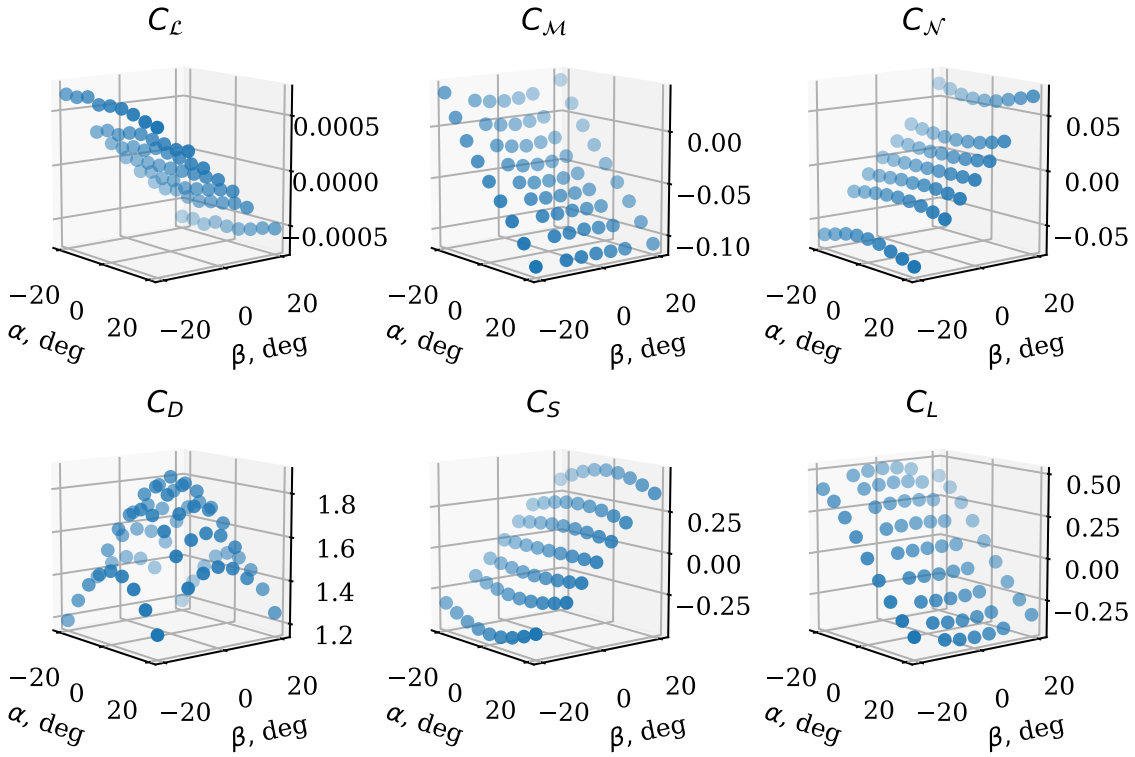

Figure 4: Aerodynamic force and moment coefficients for the base aeroshell as functions of angle-of-attack and sideslip for $M = 40$

large variability, the magnitudes are very small and are an artifact of numerically differentiating the small roll moment coefficients that are on the order of 10^{-3}. The sign of the derivative, and therefore the stability in the lateral direction, does not change as expected from visual inspection of Figure 6. Figures 10 and 11 depict negative pitch stiffness indicating longitudinal stability and positive yaw stiffness demonstrating directional stability, respectively. Thus, the vehicle is statically stable in the hypersonic entry regime of interest. In the next section we detail the control design to utilize the control surfaces to follow guidance commands.

CONTROL DESIGN

We design a linear state-feedback controller based on the Linear Quadratic Regulator (LQR) method from optimal control theory.[6] The LQR method is selected because of its strong performance characteristics. In addition, the LQR control design technique allows for the relative allocation of control effort and tracking performance for each variable through the choice of weighting matrices in the cost function. Thus, we can specify which and how much of the eight control surfaces to use.

Since the control system will be tracking attitude commands, we model the vehicle state as

$$x = [p\ q\ r\ \sigma\ \alpha\ \beta\ e_\sigma\ e_\alpha\ e_\beta]^T$$

which is the angular velocity and wind attitude variables augmented by the integral error state

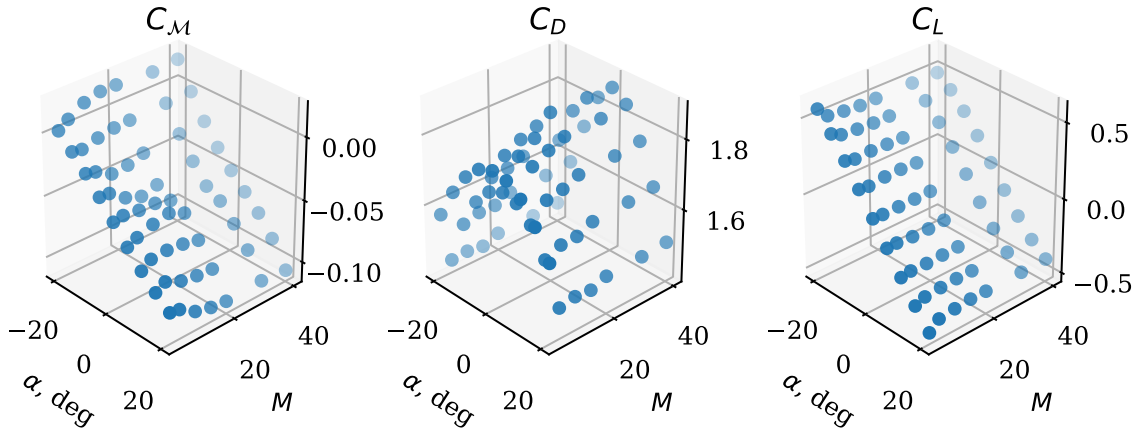

(a) Longitudinal aerodynamic force and moment coefficients for the base aeroshell as functions of angle-of-attack and Mach for $\beta = 0\,\text{deg}$

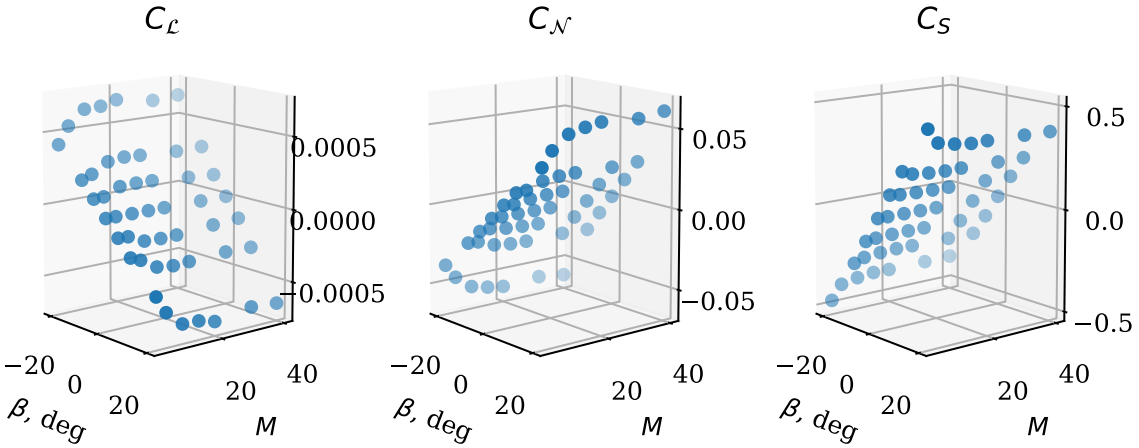

(b) Lateral and directional aerodynamic force and moment coefficients for the base aeroshell as functions of sideslip and Mach for $\alpha = -15\,\text{deg}$

Figure 5: Aerodynamic force and moment coefficients dependence on Mach

variables e_σ, e_α, and e_β. This augmentation is done to reduce steady-state errors between the actual and commanded bank, angle-of-attack, and sideslip. The derivatives for the integral error state variables are given by

$$\dot{e}_\sigma = \sigma - \sigma_c$$
$$\dot{e}_\alpha = \alpha - \alpha_c$$
$$\dot{e}_\beta = \beta - \beta_c$$

where α_c, β_c, and σ_c are the commands from guidance.

The system control inputs

$$u = [\delta_1 \; \delta_2 \; \cdots \; \delta_8]^T$$

are the hinge deflection angles of the eight aerodynamic control surfaces into or out of the flow, as defined above.

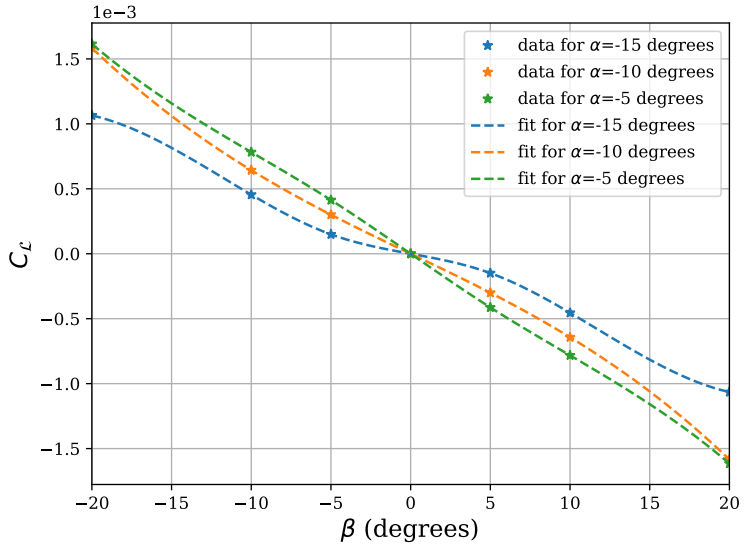

Figure 6: Roll moment coefficient $C_{\mathcal{L}}$ as a function of β for various α, $M = 40$ and $\delta_1 = \delta_2 = \cdots = \delta_8 = 0\,\text{deg}$

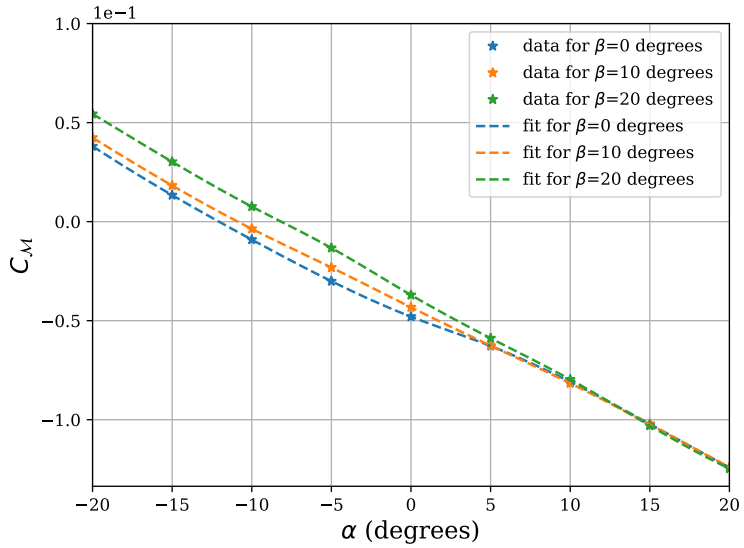

Figure 7: Pitch moment coefficient $C_{\mathcal{M}}$ as a function of α for various β, $M = 40$ and $\delta_1 = \delta_2 = \cdots = \delta_8 = 0\,\text{deg}$

To develop the linear controller, we linearize the equations of motion, for the states defined above, at the desired point in the flight envelope to obtain state-space linear equations of the form

$$\Delta\dot{x} = A\,\Delta x + B\,\Delta u$$

where Δx and Δu are deviations from the linearization point x^*, u^*. The matrices A and B defined

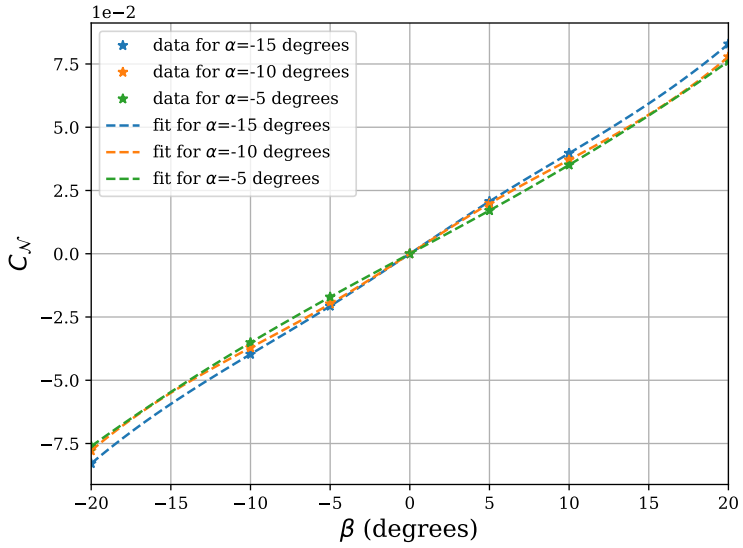

Figure 8: Yaw moment coefficient $C_{\mathcal{N}}$ as a function of β for various α, $M = 40$ and $\delta_1 = \delta_2 = \cdots = \delta_8 = 0\,\text{deg}$

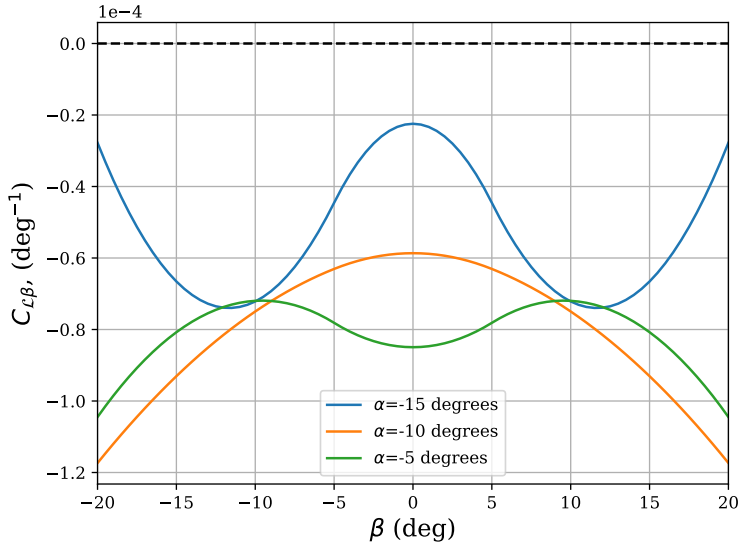

Figure 9: Dihedral derivative $C_{\mathcal{L}\beta}$ as a function of β for various α, $M = 40$ and $\delta_1 = \delta_2 = \cdots = \delta_8 = 0\,\text{deg}$

by

$$A = \left.\frac{\partial f}{\partial x}\right|_{x^*,u^*} \qquad B = \left.\frac{\partial f}{\partial u}\right|_{x^*,u^*}$$

are called the state and input matrices respectively. Here, $f(x, u)$ is the vector-valued function of the derivatives for each state variable concatenated together.

The linearization point is chosen by assuming perfect tracking, steady-state conditions, symmet-

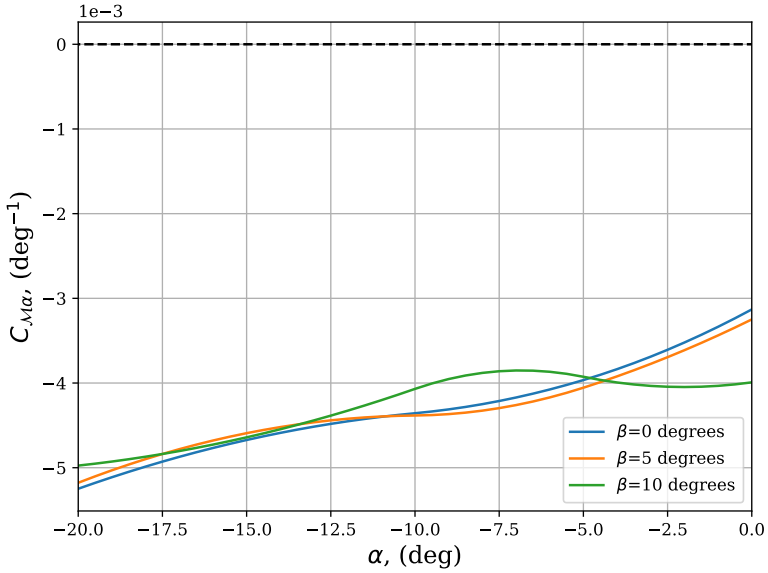

Figure 10: Pitch stiffness $C_{\mathcal{M}\alpha}$ as a function of α for various β, $M = 40$ and $\delta_1 = \delta_2 = \cdots = \delta_8 = 0\,\text{deg}$

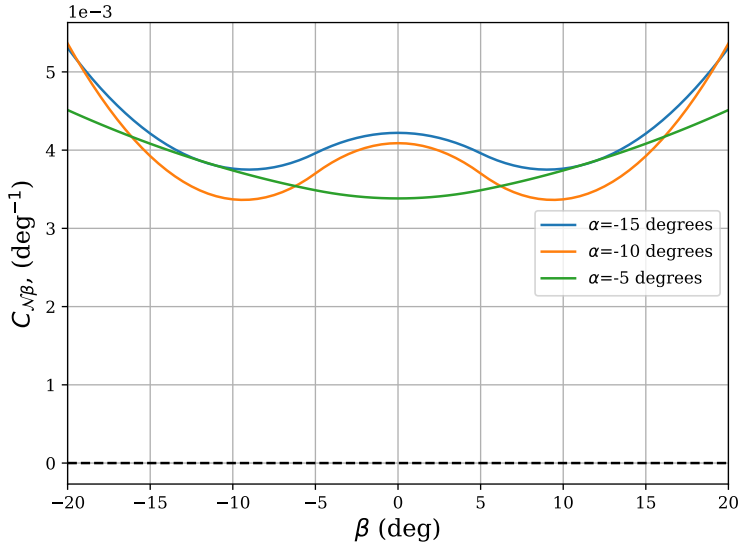

Figure 11: Yaw stiffness $C_{\mathcal{N}\beta}$ as a function of β for various α, $M = 40$ and $\delta_1 = \delta_2 = \cdots = \delta_8 = 0\,\text{deg}$

ric nominal control surface deflections, and trim angle-of-attack from a Newton-Raphson solver. The control system is designed at a Mach number of 40 where the guidance and control systems are activated for a notional lunar return mission, described in a previous report.[2] This leads to the conditions listed in Table 2.

Using these linearized dynamics, the LQR control law is given by

$$u = u^* - K\,\Delta x$$

Table 2: Linearization point for control system design

variable	values
Mach number, M	40
dynamic pressure, $\overline{q}$ Pa	220
angular velocity, p^*, q^*, r^*, deg/s	0
sideslip angle β^*, deg	0
bank angle σ^*, deg	0
control surface deflection δ_i^*, deg	-30
angle-of-attack α^*, deg	-14.5
integral error, e_σ^*, e_α^*, e_β^*, deg·s	0

where K is the feedback gain matrix. The feedback gain is computed to minimize the quadratic cost function

$$J = \int_0^\infty \Delta x^T(\tau)\, Q\, \Delta x(\tau) + \Delta u^T(\tau)\, R\, \Delta u(\tau)\, d\tau$$

where Q and R are tunable weighting matrices for the states and control surfaces respectively. The gain matrix that minimizes the cost function for a particular linear system can be found using a number of numerically stable algorithms by constructing the appropriate Algebraic Riccati Equation or Linear Matrix Inequality.[7]

SIMULATION RESULTS

To evaluate the controller, we simulate the nonlinear equations of motion for the state of the vehicle and the linear state-feedback controller using a Python-based simulation framework.[8] For these simulations, the states are initialized at the linearization point with a constant Mach number of 40, described in the previous section. We evaluate the ability of the controller to track guidance commands of angle-of-attack and sideslip for a fixed bank angle. We also investigate the trimmable range of angle-of-attack and sideslip. as described below.

Trimmability study

We performed a trimmability study in order to understand the full limits of the control system to track α/β guidance commands. In this study, a number of simulations were performed with combined step commands in angle-of-attack and sideslip, with the same simulation conditions as described above. In Figure 12, we plot the commanded angle-of-attack and sideslip with the corresponding final, steady-state controlled counterparts, with the two connected by a black line. Simulations with large commands in either angle-of-attack or sideslip have relatively small steady state errors. Simulations with large angle-of-attack and sideslip commands result in larger steady state errors. In the subsequent subsections, we present step responses to angle-of-attack and sideslip commands from this study and discuss sideslip limits due to roll-yaw coupling.

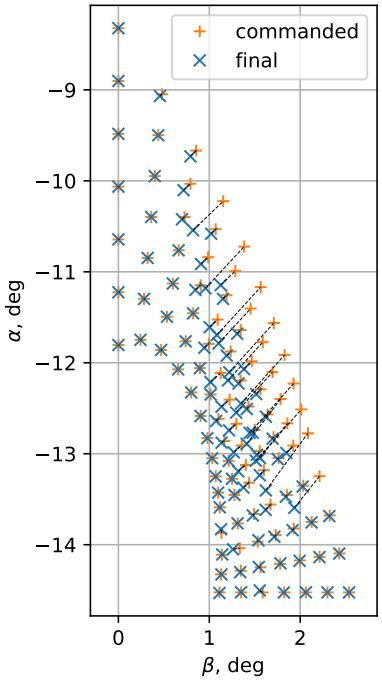

Figure 12: Plot of commanded and steady-state angle-of-attack and sideslip for trimmability study

Angle-of-attack step commands In Figures 13 and 14, we show the simulation results for two of the pitch-up angle-of-attack step commands, -4.3 degrees and -2.5 degrees respectively, from the initial trim of -14.5 degrees. The bank and sideslip angles are commanded to be zero. Commands are shown in dashed black lines, while the time history of the controlled state variables is shown in solid lines. In Figure 13, the control system is able to drive the vehicle to the commanded attitude by moving the top tabs into the flow and the bottom tabs out of the flow, with most tabs saturating. In Figure 14, the control system cannot achieve the commanded angle-of-attack because all tabs saturate at the +20 degree or -45 degree mechanical limits, demonstrating the control authority limits of the system.

Sideslip step commands In Figures 15 and 16, we show simulation results for the sideslip step commands of 2.8 degrees and 4.2 degrees, respectively, from an initial trim of 0 degrees. The bank angle and angle-of-attack are commanded to be zero and the trim value of -14.5 degrees, respectively. Commands are shown in dashed black lines, while the time history of the controlled state variables is shown in solid lines. In Figure 13, the control system is able to drive the vehicle to the commanded sideslip. In Figure 14, the control system does not achieve the commanded sideslip angle. In both cases, the control surface deflections do not match the intuition developed based on the sign of the induced moments. Based on the step response of the angle-of-attack commands, one would expect the left tabs numbered 1, 6, 5, and 8 to deflect fully into the flow and the right tabs numbered 2, 3, 4, and 7 to retract out of the flow to induce the largest negative yaw moment magnitude, as discussed in the vehicle overview. However only tabs 7, 5, and 8 follow this pattern, with tabs 1 and 6 saturating in the opposite direction. To investigate this unexpected observation, we look at the moments that are induced on the vehicle at non-zero sideslip angles, independent of the control system design.

Aerodynamic Moments Effects on Trimmability To understand the sideslip trimmability limits, we plot the aerodynamic roll, pitch, and yaw moment coefficients for the vehicle in Figures 17 – 19, respectively, for four different configurations: the full pitch-up (top tabs fully into flow, bottom tabs fully out of flow), full pitch-down (top tabs fully out of flow, bottom tabs fully into flow), yaw-left (left tabs fully into flow, right tabs fully out of flow), and full yaw-right (left tabs fully out of flow, right tabs fully into flow.)

The maximum angle-of-attack that the vehicle can hold can be interpreted using the pitch moment coefficient curves shown in Figure 18. In the full pitch-up tab configuration, the pitch moment coefficient, and therefore the pitch moment, is zero near $\alpha = -3.5\,\mathrm{deg}$. Since this is where the pitch moment is zero in the full pitch-up configuration, this is the maximum trimmable angle-of-attack. This value is in between the achievable and unachievable commands of Figures 13 and 14.

However, the maximum trimmable sideslip is not as straightforward. Based on the yaw moment coefficient shown in Figure 19, one might expect a maximum achievable sideslip angle close to 18 degrees, where the yaw moment coefficient vanishes in the full yaw-left tab configuration. However, for this sideslip angle of 18 deg and full yaw-left tab configuration, there is negative roll moment coefficient for the vehicle, as depicted in Figure 17. In order to trim the induced roll moment, the control system must generate a positive roll moment. In Figure 17, at 18 deg sideslip angle, the yaw right and pitch down configurations are the configurations that induce positive roll moments on the vehicle. Moving the tabs to balance the roll moment reduces the trimmable sideslip range. This suggests that the control surface deflections shown in Figures 15 and 16 are a result of the controller attempting to drive the sideslip to the commanded angle while trimming the induced roll moment due to sideslip.

CONCLUSION

In this paper, we presented a mathematical model of the LNA deployable entry vehicle, evaluated the static stability of the vehicle, developed an LQR controller, and showed initial results tracking step commands. The LQR controller was able to find the control surface deflections required to hold the commanded attitude within the trimmability limits. This control design methodology is a useful starting point for hypersonic entry vehicles using aerodynamic control surfaces.

REFERENCES

[1] A. Cassell, B. Smith, P. Wercinski, S. Ghassemieh, K. Hibbard, A. Nelessen, and J. Cutts, "ADEPT, A Mechanically Deployable Re-Entry Vehicle System, Enabling Interplanetary CubeSat and Small Satellite Missions," *32nd Annual AIAA/USU Conference on Small Satellites*, Utah, SSC18-XII-08, August 2018.

[2] S. N. D'Souza, W. A. Okolo, B. E. Nikaido, B. C. Yount, J. Tran, B. W. L. Margolis, B. P. Smith, A. M. Cassell, B. J. Johnson, K. E. Hibbard, J. D. Barton, and Z. Hays, "Developing an Entry Guidance and Control Design Capability using Flaps for the Lifting Nano-ADEPT," *AIAA Aviation and Aeronautics Forum and Exposition*, 2019.

[3] N. X. Vinh, A. Busemann, and R. D. Culp, *Hypersonic and Planetary Entry Flight Mechanics*. The University of Michigan Press, Ann Harbor, 1980.

[4] M. Aftosmis, M. Berger, and G. Adomavicius, "A parallel multilevel method for adaptively refined Cartesian grids with embedded boundaries," *38th Aerospace Sciences Meeting and Exhibit*, 2000, p. 808.

[5] C. d. Boor, *A Practical Guide to Splines*. Springer, 1978.

[6] D. E. Kirk, *Optimal control theory: an introduction*. Prentice Hall, New Jersey, 1970.

[7] S. Boyd, L. El Ghaoui, E. Feron, and V. Balakrishnan, *Linear matrix inequalities in system and control theory*, Vol. 15. Siam, 1994.

[8] B. W. Margolis, "SimuPy: A Python framework for modeling and simulating dynamical systems," *The Journal of Open Source Software*, Vol. 2017, 2017.

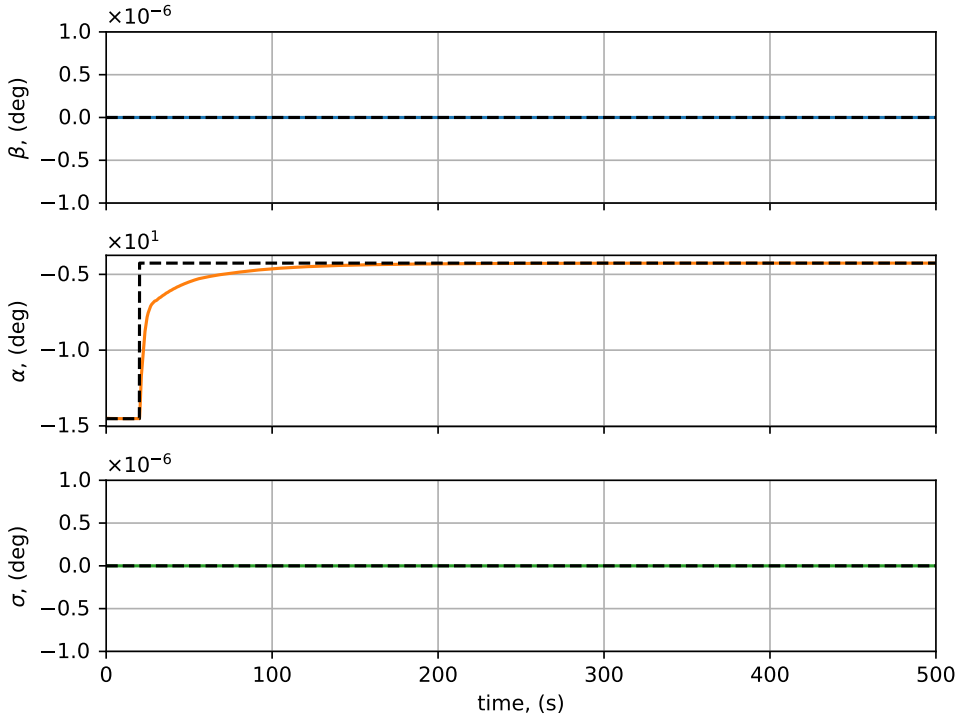

(a) Attitude

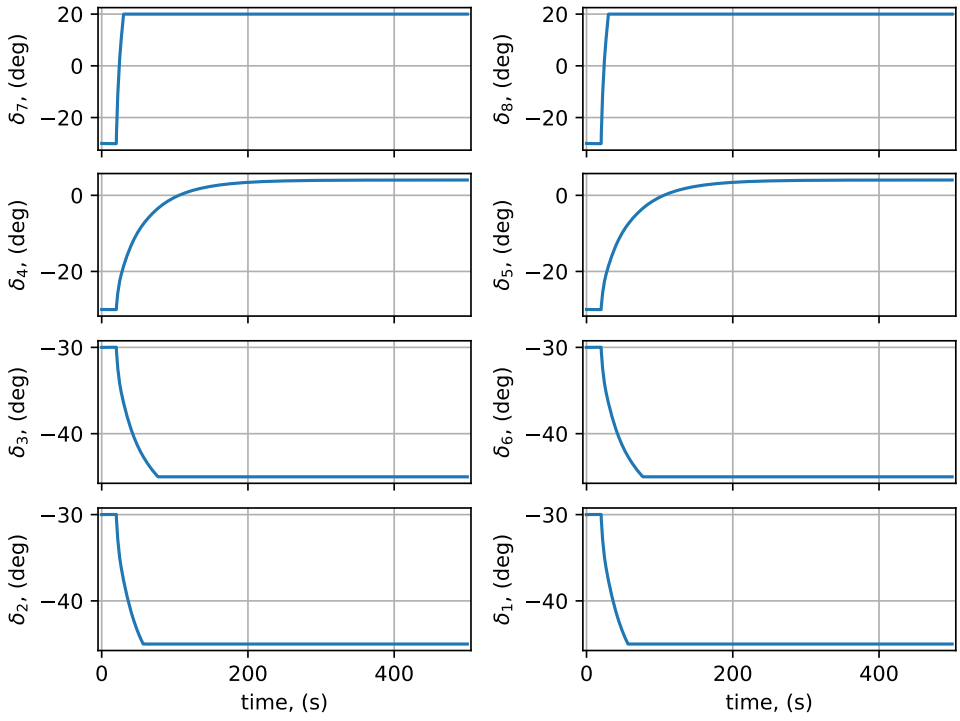

(b) Control surface deflection

Figure 13: Simulation results for achievable step command in angle-of-attack

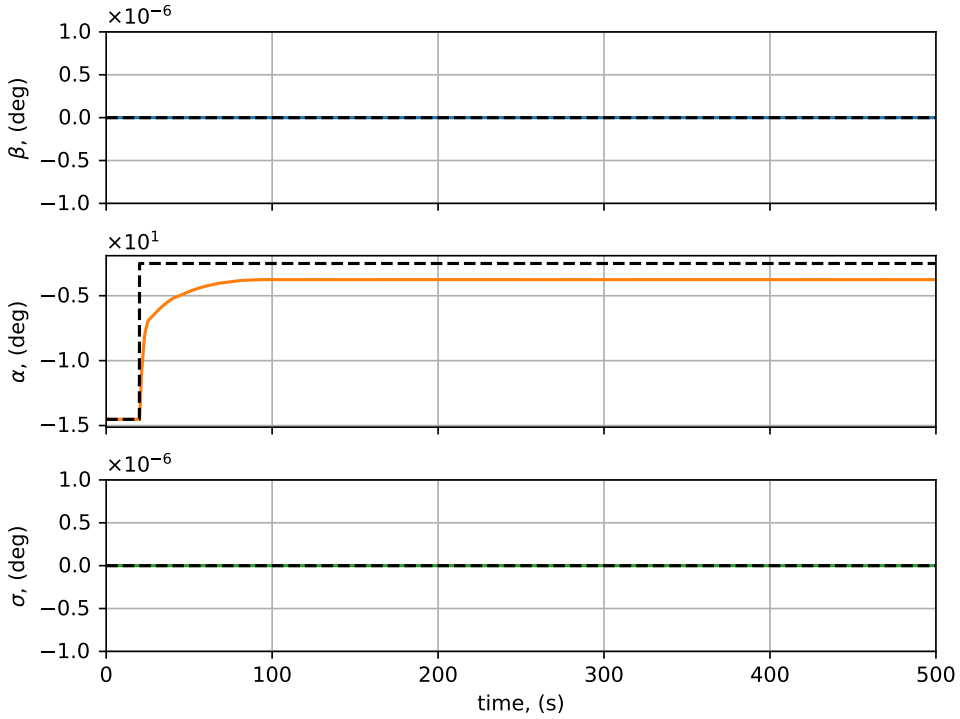

(a) Attitude

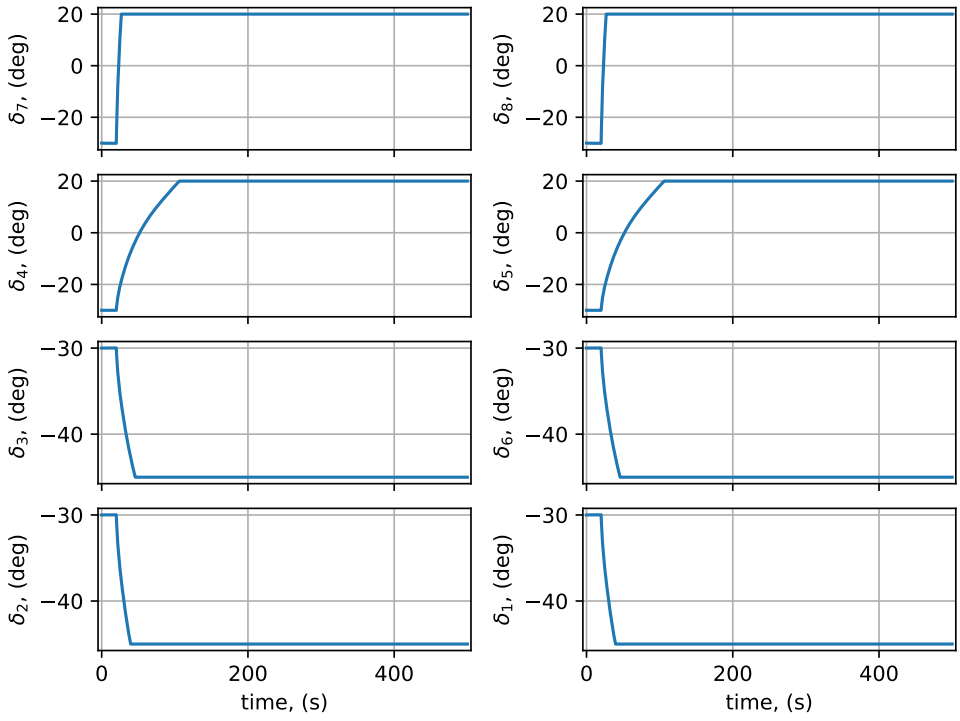

(b) Control surface deflection

Figure 14: Simulation results for unachievable step command in angle-of-attack

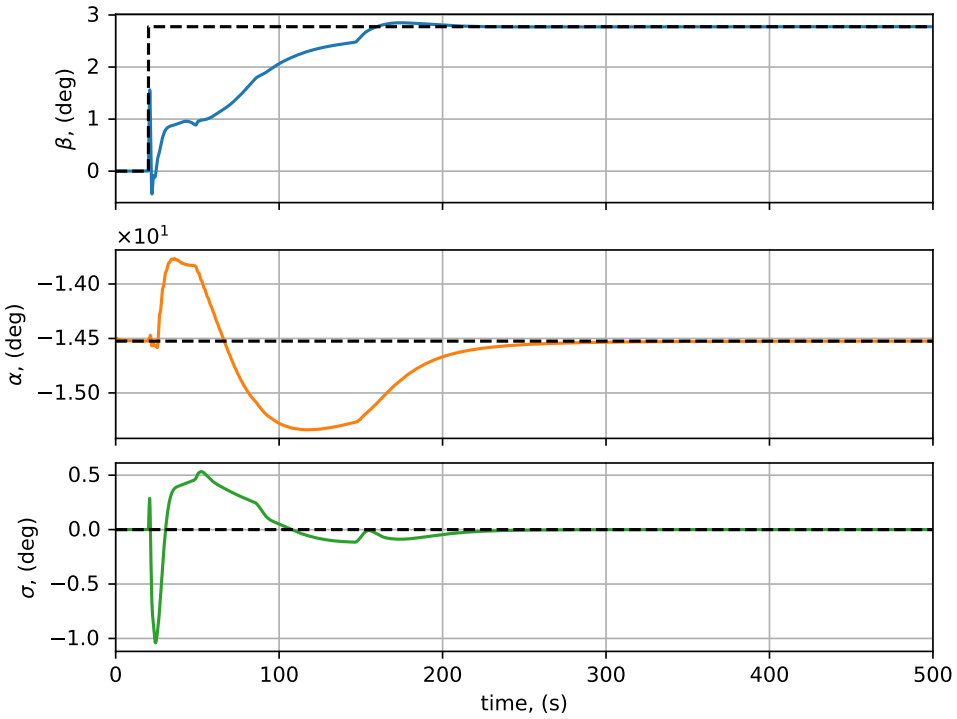

(a) Attitude

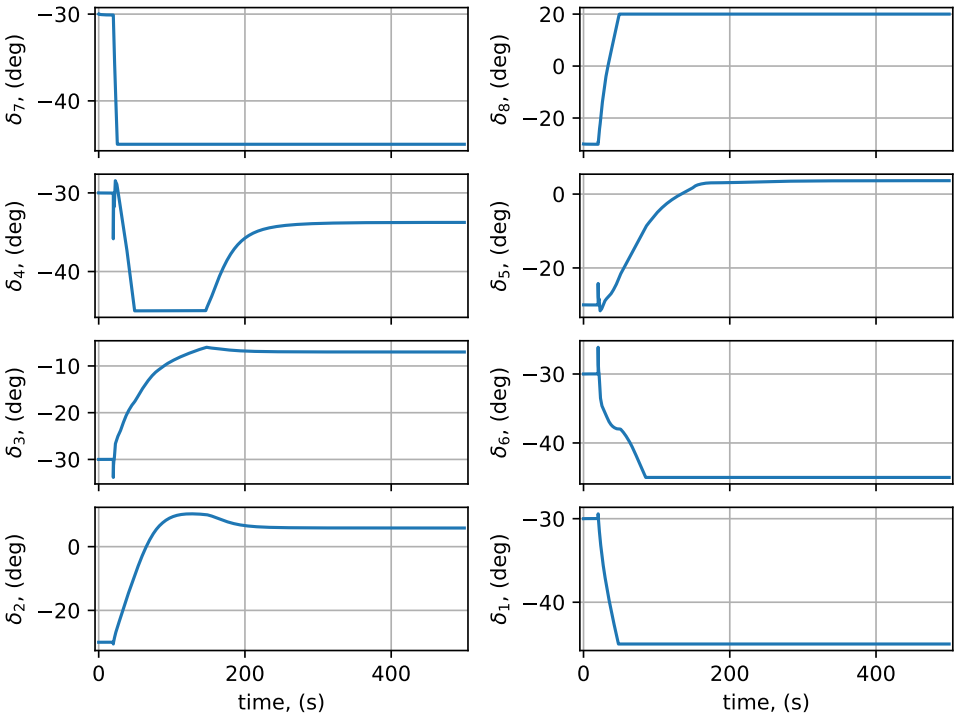

(b) Control surface deflection

Figure 15: Simulation results for achievable step command in sideslip angle

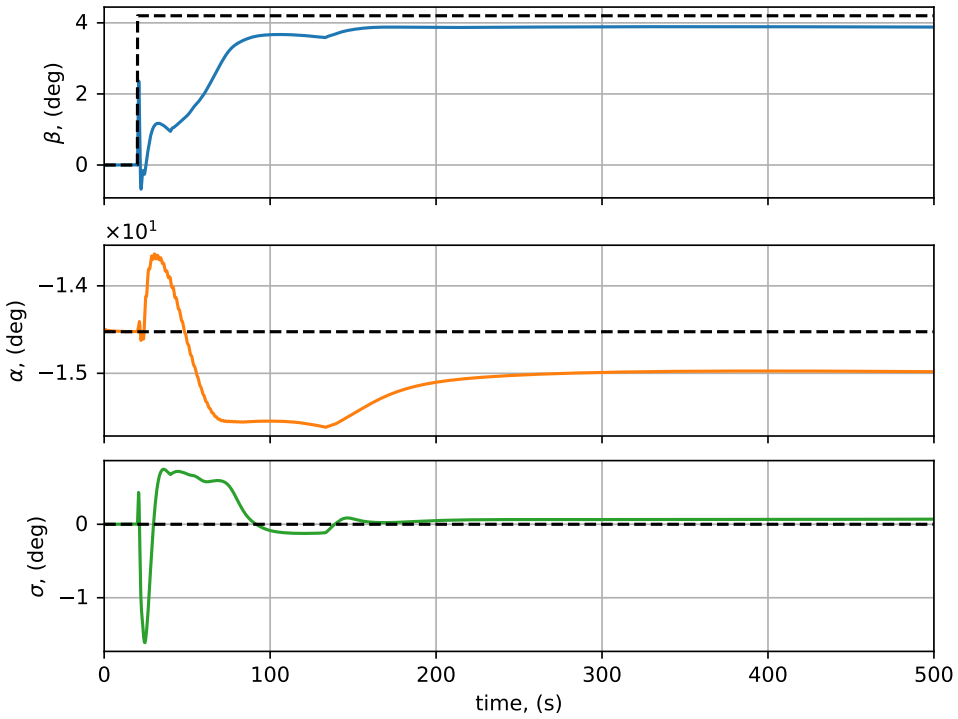

(a) Attitude

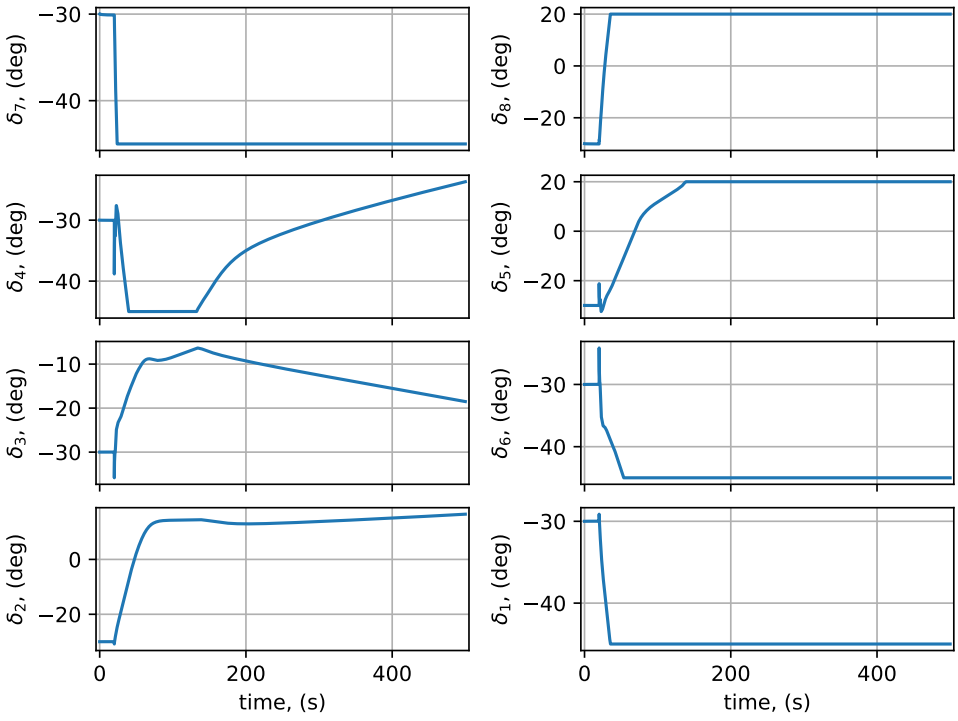

(b) Control surface deflection

Figure 16: Simulation results for unachievable step command in sideslip angle

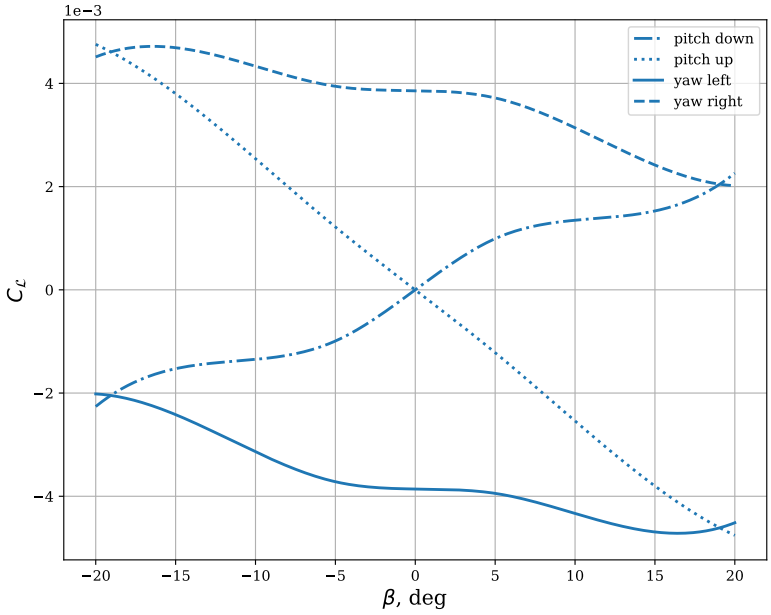

Figure 17: Roll moment coefficient $C_{\mathcal{L}}$ for the vehicle as a function of β for various tab configurations at $\alpha = -15\,\mathrm{deg}$ and $M = 40$

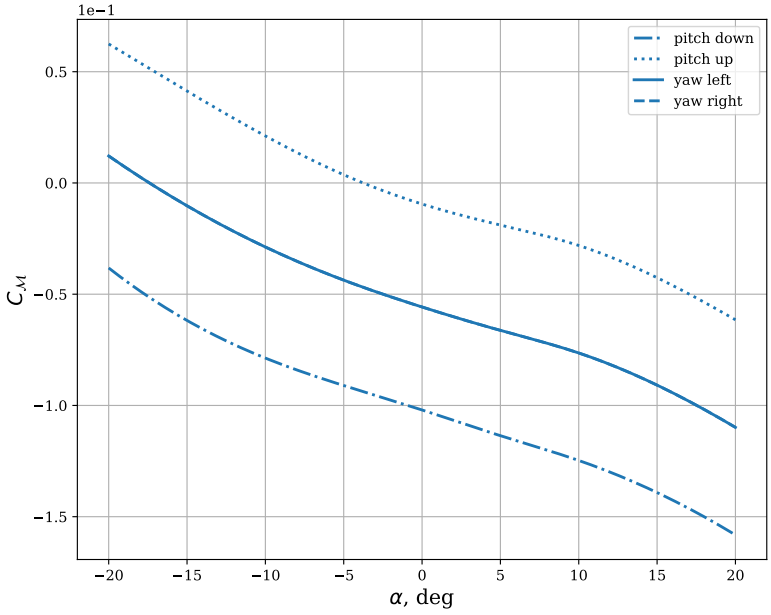

Figure 18: Pitch moment coefficient $C_{\mathcal{M}}$ as a function of α for various tab configurations at $\beta = 0$ and $M = 40$

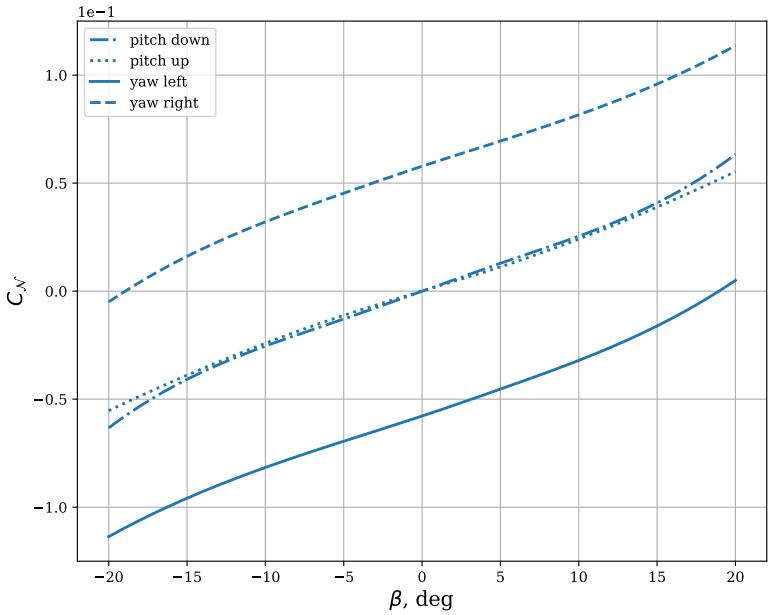

Figure 19: Yaw moment coefficient $C_{\mathcal{N}}$ as a function of β for various tab configurations at $\alpha = -15\,\text{deg}$ and $M = 40$